- 1 Benthic deposition and burial of total mercury and methylmercury estimated using thorium
- 2 isotopes in the high-latitude North Atlantic
- 3 Xiangming Shi\*1,2, Amber L. Annett<sup>3</sup>, Rhiannon L. C. Jones<sup>3</sup>, Rob Middag<sup>4,5</sup>, Robert P. Mason<sup>2</sup>
- <sup>1</sup>Polar and Marine Research Institute, Jimei University, Xiamen 361021, China.
- <sup>2</sup>University of Connecticut, Department of Marine Sciences, 1084 Shennecossett Road, Groton, CT, 06340
- 6 USA.
- <sup>3</sup>University of Southampton, Waterfront Campus European Way, Southampton, SO14 3ZH UK.
- <sup>4</sup>Royal Netherlands Institute for Sea Research (NIOZ), Department of Ocean Systems, 1790 AB Den Burg,
- 9 The Netherlands.
- <sup>5</sup>Centre for Isotope Research Oceans, University of Groningen, PO Box 72, 9700 AB Groningen, The
- 11 Netherlands

13

14

15

16

17

18

19 20

21

22

23

24

25

26

27

28 29

30

31

### Abstract

The high-latitude oceans are regions of high mercury (Hg) bioaccumulation, especially as methylmercury (MeHg), which is of great concern in terms of human and ecosystem health. In the high-latitude North Atlantic (60-80°N), the deep water entrains the Hg-enriched Arctic water southwards, consequently influencing global Hg cycling. Whilst Hg removal has been proposed en route from the Arctic Ocean to the Atlantic Ocean, the factors and the mechanism underpinning this loss are poorly studied. Here, we constrain Hg behavior at the sediment-water interface during the GEOTRACES process study GApr16 in 2021 using radionuclide approaches. Excess thorium isotopes (234Thex and 228Thex) in the sediment evidence significant sediment resuspension and redeposition on top of the shallow shelves and sills due to the intense overflows. The benthic deposition and burial fluxes of Hg species were then evaluated based on <sup>234</sup>Th<sub>ex</sub> and <sup>228</sup>Th<sub>ex</sub>, respectively. This analysis showed that most of the total Hg deposited from the bottom water was buried into the sediment. The net scavenging flux was  $14.8 \pm 7.0 \,\mathrm{Mg} \,\mathrm{y}^{-1}$ , explaining half of the Hg removal proposed in previous studies. In comparison, the benthic scavenging flux of MeHg was  $27 \pm 10 \text{ kg y}^{-1}$ . Due to the lower particle activity, MeHg deposited from the bottom water is not retained well in the sediment, and over half was estimated to be released, mainly by diffusion and advection, to the water column. This efflux might account for some MeHg hotspots in the subsurface water. Overall, benthic scavenging dominated the Hg loss from the water column of the high-latitude North Atlantic with the shallow shelves and sill regions being the primary deposition zones.

32 33 34

Keywords: Deposition flux; Burial flux; Methylmercury; North Atlantic; Thorium isotopes

35 36

37

38

39 40

Geochimica et Cosmochimica Acta

### 1. Introduction

Mercury (Hg) is a toxic element, especially as one of its species, the neurotoxin methylmercury (MeHg, CH<sub>3</sub>Hg), that can bioaccumulate in organisms through the food chain. The toxicity is particularly magnified in aquatic food webs, leading to human exposure and the degradation of environmental health (Davidson et al., 2000; Grandjean et al., 1997; Jensen and Jernelöv, 1969). Although anthropogenic Hg release has been somewhat controlled and limited since the Minamata mercury poisoning event, anthropogenic Hg still exists within the ecosystem as "legacy Hg" which is a potential pollutant source that can return Hg from sediments and other reservoirs to the biogeochemical cycle in the ocean (Driscoll et al., 2013; Lamborg et al., 2014).

Mercury is of particular concern in the Arctic where Hg concentrations in marine biota have increased by an order of magnitude since the industrial revolution (Dietz et al., 2009). The annual polar spring Hg depletion due to atmospheric chemical transformation of elemental Hg to ionic Hg deposits considerable atmospheric Hg to the Arctic Ocean (Dastoor et al., 2022). This input has increased with global warming as Hg delivery to Arctic waters is enhanced by loss of sea-ice and melting of ice sheets (Araujo et al., 2022; DiMento et al., 2019). Additionally, as Hg is concentrated in the Arctic waters and transported south to the North Atlantic where deep water forms, there is potential for this Hg to be transported to lower latitudes (Soerensen et al., 2016; Soerensen et al., 2010; Zhang et al., 2020). Petrova et al. (2020) concluded that both total Hg and MeHg were exported from the Arctic Ocean to the North Atlantic based on concentration differences between the endmember water masses. As the thermohaline circulation conveys the deep water from the high-latitude North Atlantic globally, Hg behavior in the "gateway zone" of deep water formation has an inevitable impact on global Hg cycling via the Hg transport into the deep ocean (Amos et al., 2013; Mason et al., 1995; Sunderland and Mason, 2007). However, there are additional potential pathways of Hg addition to these waters from coastal and sediment sources or Hg removal due to scavenging and particle settling during transit. To date studies in other Arctic regions have suggested that sediments can be not only a sink but also a Hg source (Soerensen et al., 2016 and references therein) but few studies have examined the benthic processes on Hg and MeHg cycling in these gateway regions.

Recent studies completed as part of the GEOTRACES program have investigated oceanographic sections near Fram Strait and the Greenland-Iberian transect (GA01) to quantify the Hg budget between the Arctic and the North Atlantic Oceans (Bowman et al., 2015; Cossa et al., 2018; Petrova et al., 2020). Along the East Greenland Current (EGC), the Hg flux southward via the Fram Strait from the Arctic Ocean was higher than that for water crossing 60°N (transects 1 and 3 in the left panel of Fig. 1). Along the North Atlantic Current (NAC) which flows northward, the Hg flux crossing the North Atlantic (transect 3) was higher than the sum of the inflows to the Arctic Ocean via the Fram Strait and Barents Sea Opening (transects 1 and 2). The Hg imbalance in the northward and southward currents suggests that some Hg has been scavenged from these water masses when transiting the high-latitude North Atlantic (60-80°N). However, Hg behavior and biogeochemical processes during the transit are understudied: there are few studies on benthic Hg burial in the ridge regions, and the estimation of mercury export flux

on the Greenland and Barents Sea shelves has high uncertainties (Mason et al., 1995; Soerensen et al., 2016; Tesán Onrubia et al., 2020).

81

82

83

84

85

86

87 88

89

90

91

92

93

94

95

96

97

98

99

100

101

102

103

104

105

106

107

108

109

110

111

112

113

114

115

116

117

118

119 120

121

122

The Greenland-Iceland-Faroes Ridge is the shallowest region where both the EGC and NAC must pass in the North Atlantic. As Hg is particle reactive in the ocean, the sediment-water exchange processes likely have an important impact on the degree of Hg scavenging considering that the deep water is the primary carrier of the high-Hg Arctic water southward. The sediments of a shallow ridge can be disturbed and resuspended by an intense overflow. These particles could then adsorb Hg from the water column prior to redeposition to the sediments. Alternatively, there could be a net release of Hg from sediment due to resuspension, dissolved efflux and sedimentary transformations. Understanding and quantifying the benthic processes are vital to clarify the mechanism of Hg scavenging in the gateway zone. Hence, a new approach, the presence of "excess short-lived thorium isotopes", was introduced to quantify Hg deposition and burial to the sediment in this region. Thorium (Th) is also particle reactive and has two short-lived isotopes <sup>234</sup>Th and <sup>228</sup>Th, with half-lives of 24.1 days and 1.91 years, respectively. Their parents, uranium-238 (<sup>238</sup>U) and radium-228 (<sup>228</sup>Ra), are dissolved and less particle-reactive than Th in seawater. When particle resuspension-redeposition occurs at the sediment-water interface, Th is quickly scavenged onto the precipitating particles due to its strong affinity to particle surfaces. This external input from the water column leads to a Th excess in the surface sediment relative to that predicted from the "parent" concentration, providing a means to quantify the particle scavenging near the seafloor (Rutgers van der Loeff et al., 2002; Tamborski et al., 2022; Xu et al., 2015). Moreover, the predictive timescales based on these two isotopes <sup>234</sup>Th and <sup>228</sup>Th (<1 month to ~10 years) coincide with the current transit time of water from Fram Strait into the Irminger Sea such as the EGC (months to a couple of years, Foukal et al., 2020).

The GEOTRACES process study (GApr16) provided a unique opportunity to examine the potential importance of sediments on Hg transport and fate between the North Atlantic and Arctic Oceans. The investigation covered the shelf-slope zones around Iceland with sections across the full Greenland-Iceland-Faroes Islands ridge where the bottom hosts nepheloid layers induced by the high kinetic energy due to the high current flow (Gardner et al., 2018). The earlier GEOTRACES program studies mapping <sup>234</sup>Th distributions (the GA02 section) has shown that the <sup>234</sup>Th-<sup>238</sup>U were at equilibrium below 200 m in the subpolar Irminger Sea (Le Gland et al., 2019; Puigcorbé et al., 2017), indicating that the influence of <sup>234</sup>Th scavenged from the euphotic zone is negligible in terms of contributing to the excess <sup>234</sup>Th at the surface sediment when water depth is over 200 m. A benthic nepheloid layer was found over the Yermak Plateau (water depth <1000 m) of the Fram Strait. Meanwhile, <sup>234</sup>Th depletion relative to <sup>238</sup>U was observed in the near-bottom water and excess <sup>234</sup>Th was observed in the sediment (Rutgers van der Loeff et al., 2002). suggesting that the excess <sup>234</sup>Th of the surface sediment was derived from the deposition of bottom suspended particles. Similarly, such thorium excess likely occurs in the Denmark Strait and Faroe Bank Channel (the right panel of Fig. 1) when particle deposition scavenges Th from bottom water. Hence in this study, we used Th isotope signatures to estimate Hg deposition flux and burial flux, quantifying the extent of Hg scavenging at the sediment-water interface and illuminating the role of sediment in the loss mechanism for Hg in the regions around Iceland. Specifically, in this paper, the term "deposition flux" refers to the amount of particulate mercury added to the sediment surface with the deposition of resuspended particles per unit area per unit time (mol m<sup>-2</sup> d<sup>-1</sup>); and the "burial flux" represents the amount of particle mercury delivered downcore below the sediment surface per unit area per unit time (mol m<sup>-2</sup> d<sup>-1</sup>).

- 2. Method
- 128 2.1 Study area and background

The GEOTRACES process study GApr16 aimed to unravel the role of trace metals in the high latitude North Atlantic (60-70°N) which is the gateway zone between the North Atlantic and Arctic Oceans. Sampling was carried out on RV Pelagia from July 18th to August 16th 2021 around Iceland. Most sediment sites were located on the Greenland shelf beneath the EGC, or on the top of the Greenland-Iceland ridge in the Denmark Strait (the right panel of Fig. 1). The northernmost sediment site (Station 21) is near the outlet of Scoresby Sound where glacial ice is released and a considerable amount of sediment is entrained into the ocean (Hasholt et al., 2022). Stations 8 and 10 are on the Greenland shelf break where water depth is >1000 m. Stations 15/16/17/21 are all on the shelf with a water depth of 300 ~ 800 m (details in Appendix Table S1). On the east side of Iceland, Station 30 is in the Faroes-Shetland Channel and Station 36 is close to the Iceland-Faroe Ridge. 

Although multiple currents meet near Iceland (Hansen and Østerhus, 2000; Hansen et al., 2003), here we only consider the overflows near the seafloor in light of the influence of benthic processes on Hg cycling. Along the Denmark Strait, the cold and dense EGC overflow, regarded as the largest contributor to lower North Atlantic Deep Water, passes the Greenland-Iceland ridge southward at a rate of >3.0 Sv (Dickson and Brown, 1994; Lin et al., 2020). The flow rate decreases over the shelf break so the sediment nearby is dominated with clay and silt (Stations 15/17). On the east side of the strait, the northward-flowing North Icelandic Irminger Current (NIIC) passes through the trough where the hard packed sediment and strong bottom current led to the failure of recovering sediment cores (Station 14). Stations 30 and 36 are located on the southeast of Iceland, on the pathway of two other main overflows: one passes the Faroe Bank Channel at a rate of approximate 2.0 Sv and the other crosses the Iceland–Faroe Ridge at a rate of ~1.0 Sv (Beaird et al., 2013; Østerhus et al., 2008). The sediment of Station 30 is dominated by fine silt as it is on the north of the ridge, receiving particles entrained from the Shetland shelf. The sandy sediment found at Station 36 could be a result of fine particle removal by bottom currents.

### 2.2 Sample collection

Sediment cores were collected with a 12-tube multicorer (Oktopus). After being retrieved intact (assessed visually by an undisturbed sediment-water interface with clear overlying water, and relatively flat sediment surface), all core top water was siphoned out of the tubes and collected into a clean cubitainer (20 L). The sediment cores were sliced for subsamples: one third of each slice for <sup>224</sup>Ra-<sup>228</sup>Th analysis and the remainder for porosity and excess <sup>234</sup>Th. Subsamples for <sup>224</sup>Ra-<sup>228</sup>Th were processed onboard immediately and the full processing followed Cai et al. (2015). Briefly, a volume of 150 mL of Milli-Q water was added and the sediment was stirred to form a

slurry, followed with ultrasonication to disperse the particles. After adjusting pH with concentrated ammonium hydroxide (NH<sub>3</sub>·H<sub>2</sub>O) to pH = 8-9, potassium permanganate (KMnO<sub>4</sub>, 3.0 g L<sup>-1</sup>) and manganese chloride (8.0 MnCl<sub>2</sub>·4H<sub>2</sub>O L<sup>-1</sup>) were added to form a MnO<sub>2</sub> suspension in order to adsorb all dissolved Ra from the slurry. Subsequently, the slurry was evenly filtered with a homemade sediment filtration tower onto a 142mm GFF filter which was then counted in a Radium Delay Coincidence Counter system (RaDeCC).

Sampling tubes (i.d. = 110 mm) for porewater extraction were predrilled with 3 mm (i.d.) holes, wherein four siphoned cores were used: two for radium and two for mercury species. Rhizon samplers were inserted via the holes on the tube to extract porewater at an interval of 1-2 cm. As the MeHg measurement needs a high volume for distillation, porewater from the same depths in separate cores were combined together (30-40 mL in total) and stored frozen (-20°C). Once the porewater extraction was completed, one of the cores was sliced in accordance with the porewater intervals and each slice was stored frozen in a 50 mL test tube for the analysis of solid mercury species (Shi et al., 2018).

A volume of 2 L of core top water was filtered through a pre-combusted quartz filter (25 mm) to obtain suspended particles for the particulate <sup>234</sup>Th. The same procedure was followed for the particulate mercury species. All filters were stored frozen until lab analysis. The remaining core top water was filtered through a 142-mm GF/F filter using a peristaltic pump and the outflow was connected to a column of Mn-impregnated acrylic fiber to collect the radium. The filter and the fiber were then counted using the RaDeCCs for particulate <sup>228</sup>Th.

182 2.3 Sample analysis

168 169

170

171172

173

174

175

176

177

178

179

180

181

200

201

2.3.1 Analysis of sediment <sup>228</sup>Th and <sup>234</sup>Th

Sediment <sup>228</sup>Th was determined using the RaDeCCs within 10 days after the sample collection 184 so that the decay of <sup>228</sup>Th and its parent <sup>228</sup>Ra can be neglected in this time frame. Details have 185 been described by Cai et al. (2012) and Shi et al. (2018). Briefly, water content of the filtered 186 sediment plates (for  $^{224}$ Ra- $^{228}$ Th analyses) was adjusted with air pumps to 30 ~ 40%. The plates 187 were sealed in home-made round holders connected to the RaDeCCs. Filled with high-purity 188 helium gas, the RaDeCCs were run for  $8 \sim 10$  hours to measure the  $^{224}$ Ra activities of the sediment 189 plates. After ~10 days, the 2<sup>nd</sup> measurement was conducted in the same RaDeCCs. The <sup>228</sup>Th 190 activities can be calculated from the two measurements with the calibration of decay and detector 191 efficiency. The initial uncertainty of <sup>228</sup>Th activity was derived from the counting standard 192 deviation, and the overall accuracy was well controlled within  $\pm$  5% after error propagation. 193 Thorium-228 measured with the RaDeCCs is the portion bound on the surface of sediment grains 194 as the RaDeCCs can only detect α particles released from the sediment plates (Cai et al., 2012). 195 This generally includes the <sup>228</sup>Th scavenged by the precipitating particles from water column 196 (excess <sup>228</sup>Th, <sup>228</sup>Th<sub>ex</sub>) and the <sup>228</sup>Th produced from the decay of its parent in the particles 197 (supported <sup>228</sup>Th) (Tamborski et al., 2022). Excess <sup>228</sup>Th can be calculated by deducting the 198 supported <sup>228</sup>Th from the determined <sup>228</sup>Th. 199

Sediment porosity was calculated from the water content and the dried sediment was homogenized for the analysis of excess <sup>234</sup>Th (<sup>234</sup>Th<sub>ex</sub>). The pretreatment to separate and

concentrate <sup>234</sup>Th is detailed here (based on Cai et al., 2014; Hong et al., 2021). A weight of sediment (4-5 g) was digested with a mixture of hydrochloride acid (HCl, 6N) and hydrogen peroxide (H<sub>2</sub>O<sub>2</sub>, 30%) to extract thorium from sediment particles. The leachates were heated to almost dryness and then were dissolved with 10 mL of 8N nitric acid (HNO<sub>3</sub>). The extraction was transferred into a prepared anion-exchange resin column (8 cm length, AG1-X8, 100-200 mesh) for elution. The columns were purified firstly with 4×10 mL of 8N HNO<sub>3</sub> to remove most metals including iron and Ra, and 3×10 mL of 1N HCl followed to remove bismuth and to elute Th. After adjusting pH to 8-9 with NH<sub>3</sub>·H<sub>2</sub>O solution, Th-MnO<sub>2</sub> was coprecipitated from the elution using 0.375 mL of KMnO<sub>4</sub> solution (3.0 g L<sup>-1</sup>) and 0.25 mL of MnCl<sub>2</sub> solution (8.0 g L<sup>-1</sup>). The Th-MnO<sub>2</sub> particles were then filtered on a quartz filter (25 mm i.d., 2.2 µm pore size) and set on a special round holder to determine <sup>234</sup>Th in a low-level beta counter (GM-25-5, RISØ National Laboratory, Denmark). The samples of suspended particles were directly determined after drying the filter without chemical elution. The same digestion procedure and measurement were performed 6 months later when the excess <sup>234</sup>Th had fully decayed. The difference of the two determinations represents the excess <sup>234</sup>Th. In our study, the first measurement was done at the National Oceanography Center in Southampton (UK) and the second one was completed at Woods Hole Oceanography Institute (USA). All reported activities were calibrated with the detector background and efficiencies. 

# 2.3.2 Analysis of mercury species (MeHg and total Hg)

Methylmercury (MeHg) in this study was measured with a Tekran 2700 connected to an automatic sample system (Balcom et al., 2008). For the porewater and sediment samples, MeHg was first extracted by distillation after addition of 1 mL of 50% sulfuric acid and 0.5 mL of 20% potassium chloride solution (EPA, 2001). The distilled aqua was then processed for ethylation of MeHg: the pH was adjusted with potassium hydroxide (KOH, 8N) and buffered to a range of 4.6-4.9, and the MeHg in the solution was derivatized with sodium tetraethylborate (NaTEB). The ethylated mercury species was separated via a gas chromatographic column after purging and Tenax trapping. Finally, the ethylated MeHg, i.e., methylethyl Hg, was converted to Hg<sup>0</sup> with pyrolysis in argon gas and determined with cold vapor atomic fluorescence spectrometry (CVAFS) (Bloom, 1989).

Total mercury (total Hg, including all Hg species) in aqua samples was determined with a Tekran 2600 of which the detector is also CVAFS (Seelen et al., 2018). For seawater and porewater, the samples were digested with bromine chloride (BrCl) overnight to transform all mercury species into Hg<sup>II</sup>, and a water bath of 60 °C was used on porewater samples to accelerate the digestion. Then 12% hydroxylamine hydrochloride (NH<sub>2</sub>OH·HCl) was added into the digested samples to consume the remaining BrCl. Before loading samples onto the instrument, each sample was quickly amended with 0.05 mL of saturated stannic chloride (SnCl<sub>2</sub>) to convert all Hg<sup>II</sup> into Hg<sup>0</sup>, and was sealed well for the automatic analysis. Total Hg in sediment was analyzed with a Nippon direct mercury analyzer (DMA-80) by thermally decomposing all of particulate Hg to Hg<sup>0</sup> and analyzing by cold vapor atomic adsorption.

The particulate samples from the core top water were digested with 4.5 N HNO<sub>3</sub> overnight to extract the Hg species from particles (Hammerschmidt and Fitzgerald, 2006). Methylmercury was

determined using the Tekran 2700 after pH neutralization and ethylation and total Hg was measured with the Tekran 2600 as done for the aqua samples. All Hg concentrations were calibrated with field blanks and standard curves made with standard solutions (methylmercury (II) chloride, Alfa Aesar, CAS no. 115-09-3; mercury chloride, J.T. Baker, CAS no. 7487-94-7). In summary, the spike recovery from adding standard solution to samples was well controlled and >95%. The errors of reproducibility for total Hg analyses were <2%. The relative standard deviation (RSD) of duplicates for the distilled MeHg varied with the matrix: the RSD of porewater and particulate samples ranged within 3-10%, and that of sediment samples ranged from 17-30%. The average procedural blank for MeHg and total Hg was 0.25 pmol L<sup>-1</sup> and 1.21 pmol L<sup>-1</sup>, respectively.

## 2.3.3 Ancillary parameters

Total organic carbon (TOC) and total nitrogen (TN) in dried sediments and suspended particles were measured with the CHN Analyzer (EA-1108, Fisons). All samples were pretreated with acid to remove carbonates. In practice, 5 mL of HCl (1N) solution was added to ~1 g dry sediment until effervescence stopped. After removing the acid solution, the sediment was rinsed with deionized water until the pH of supernatant was neutral. The remaining solids for TOC/TN determination was dried at 60°C overnight. The filters holding suspended particles were treated via acid fuming to remove carbonates.

In this study, all nonlinear regressions for  $^{234}$ Th<sub>ex</sub> and  $^{228}$ Th<sub>ex</sub> profiles were done by the software Sigmaplot 10.0, choosing the dynamic fitting equation "Exponential Decay". The excess activity at the extinction depth was set to 0 in the regression. The R<sup>2</sup> in all the fitting curves was >0.9 and p was generally <0.05, except the one for  $^{228}$ Th<sub>ex</sub> of Station 16 (see Appendix Table S2). Specifically, the sediment depth interval that the regression involved was the upper 6 cm so that the sediment compaction can be neglected.

### 3. Results

### 3.1 Excess Th in the sediment

The sediment above 7-cm depth was analyzed for excess  $^{234}$ Th ( $^{234}$ Th<sub>ex</sub>), except for Station 36 as  $^{234}$ Th<sub>ex</sub> was too low in the sandy sediment (Fig. 2 and Appendix Table S1). The volumetric activities of  $^{234}$ Th<sub>ex</sub> in the bulk sediment are corrected with sediment density ( $\rho = 2.6 \text{ g cm}^{-3}$ ) and porosity. In order to account for the uncertainty derived from the different instruments that were used for  $^{234}$ Th counting, the errors of  $^{234}$ Th<sub>ex</sub> activities used for inventory calculation are set as  $^{36}$ C, namely three times the error that was propagated from counting statistics and other corrections (radioactive decay, detector efficiency, background, etc.). At all stations,  $^{234}$ Th was in secular equilibrium with its parent (no excess  $^{234}$ Th) below 2 cm. At Stations 8 and 10, the  $^{234}$ Th<sub>ex</sub> activities of whole profile were within the error of zero. Other stations showed significant excess  $^{234}$ Th in the top 1 cm, up to 7 dpm cm<sup>-3</sup>. The suspended particles (SPM) of the core top water had the highest  $^{234}$ Th<sub>ex</sub>, ranging from 44.6 to 226 dpm g<sup>-1</sup>, 1 ~ 2 orders of magnitude higher than the

sediment (see Appendix Table S1). Notably, here the <sup>234</sup>Th<sub>ex</sub> of SPM refers to the particulate <sup>234</sup>Th, not the total <sup>234</sup>Th in the core top water.

Being the same element, <sup>228</sup>Th exhibited a similar distribution pattern with depth (Fig. 2). Particularly for the shallow stations (water depth <800 m), the <sup>228</sup>Th profiles exhibited an exponential decrease from the top (depth = 0) to 6-cm depth. Owing to the fact that there was a relatively stable <sup>228</sup>Th in the deep sediment, we regarded these consistent <sup>228</sup>Th values as representative of the supported <sup>228</sup>Th and used the average for <sup>228</sup>Th<sub>ex</sub> calculation. For all stations, the supported <sup>228</sup>Th was ~0.1 dpm cm<sup>-3</sup> and the <sup>228</sup>Th<sub>ex</sub> depth reached 3 cm, deeper than that of the excess <sup>234</sup>Th due to the different half-lives.

# 3.2 Particulate Hg species in the sediment

At most stations, the SPM had higher Hg concentrations than the sediment (Fig. 3, Appendix Table S3) as SPM generally has higher specific surface area and Hg is particle reactive. Methylmercury in SPM ranged from 0.18 to 0.81 pmol g<sup>-1</sup> while the sediment MeHg was generally less than 0.3 pmol g<sup>-1</sup> and deceased with depth. Total Hg showed a similar distribution pattern but the concentration was ~3 orders of magnitude higher than MeHg: total Hg of SPM had a range of  $110 \sim 420 \text{ pmol g}^{-1}$  and that of sediment was mostly <100 pmol g<sup>-1</sup>. Stations 8 and 10 exhibited lower Hg concentrations in sediments (i.e., MeHg <0.07 pmol g<sup>-1</sup> and 20 ~ 65 pmol g<sup>-1</sup> of total Hg). The shallow sites close to Greenland (Stations 15, 16 and 21) exhibited higher total Hg in the sediment (110 ~ 190 pmol g<sup>-1</sup>), and the sediment even had higher Hg than the SPM at Station 21. This station is located near the outlet of Scoresby Sound and receives substantial ice and suspended particles from glacial erosion that are discharged to the nearby ocean (Hawkings et al., 2021; Overeem et al., 2017). This input may thus affect the Hg distributions and particle components from the water column to the sediment. The low SPM TOC and TN at Stations 16 and 21 (see Appendix Table S3) partly support this inference. Overall, the Hg concentrations of SPM in this study were much lower compared with the particulate total Hg of the water column on the outer shelf of the Arctic Ocean (minimum 700 pmol g<sup>-1</sup>, Tesán Onrubia et al., 2020), suggesting that the main fraction of SPM near the seafloor was not sourced from primary production in the euphotic zone. In other words, the bottom SPM contained a large fraction of particles from sediment resuspension rather than being derived from the upper water column by scavenging.

### 3.3 Dissolved Hg distributions and ancillary parameters

The Hg distributions (including MeHg and total Hg) in the dissolved phase (porewater) mirrored that in the solid phase. The lowest concentration was in the core top water, however, the maximum Hg concentrations occurred in the mid-depth of the porewater profiles, and there was a decreasing trend deeper (Appendix Table S3 and Fig. S1). Furthermore, the MeHg proportion (%MeHg) was very different between porewater and core top water. While <5% MeHg was found in porewater, the %MeHg in the core top water was 10 ~ 60%. This implies that MeHg may be not stable in these porewaters, either migrating to the water column or being degraded below the sediment-water interface (Du et al., 2019).

Station 30 had the most TOC in the sediment ( $15 \sim 35 \text{ mg g}^{-1}$ ), followed by the ridge and coastal stations (Stations 15/16/17/21). The sediment TOC at the slope stations (Stations 8/10/36) were

- 321 the lowest, generally <2 mg g<sup>-1</sup>. The sediment TN distribution patterns were the same as for TOC.
- At most stations (Stations 8/10/15/17/36), the SPM had higher C and N contents because of a
- higher specific area, but the Stations 16/21/30 exhibited a lower TN and TOC in the SPM than the
- 324 sediment (Appendix Table S3).

- 4. Discussion
- 327 4.1 Benthic deposition and sediment burial rate
- The sediments of a shallow ridge can be disturbed and resuspended by intense overflow. These
- particles then adsorb Hg from water column prior to deposition to the sediment, with scavenged
- Hg ultimately buried. This section uses <sup>234</sup>Th and <sup>228</sup>Th, with half-lives of 24.1 days and 1.91 years,
- respectively, to estimate rates of deposition, mixing, and burial.
- 4.1.1 Deposition flux estimated from <sup>234</sup>Th<sub>ex</sub>
- Strong <sup>234</sup>Th scavenging from the water column generally occurs in the euphotic zone where there is high primary production. Sinking biogenic particles can efficiently export Th owing to its
- high particle-reactivity. Although the scavenged <sup>234</sup>Th can be transported to deeper waters via
- sinking, <sup>234</sup>Th is rarely found in excess relative to its parent (<sup>238</sup>U) in deep waters owing to its short
- half-life (24.1 days) (Coale and Bruland, 1987). As previous studies around Iceland did not observe
- excess <sup>234</sup>Th in the water column below 200 m (Puigcorbé et al., 2017), we assume that at our
- sediment stations, there is no flux of scavenged <sup>234</sup>Th from the upper water column to the seafloor.
- Hence, the excess <sup>234</sup>Th observed in the surface sediment was likely sourced from the scavenging
- during sediment particle resuspension and redeposition. Indeed, previous studies have found <sup>234</sup>Th
- depletion in the bottom water of the Greenland shelf (Hein, 2010; Rutgers van der Loeff et al.,
- 343 2002), demonstrating that our assumption of the bottom water <sup>234</sup>Th source is reasonable and
- reliable. Assuming that <sup>234</sup>Th in the sediment was in steady state and the only external source was
- 345 the bottom water, the change of <sup>234</sup>Th activity can be expressed as

346 
$$\frac{\partial^{234} Th}{\partial t} = \lambda_{234}^{238} U - \lambda_{234}^{234} Th + p_{Th} = 0$$
 (1)

- where  $\lambda_{234}$  is the decay constant of <sup>234</sup>Th (0.0288 d<sup>-1</sup>) and p<sub>Th</sub> represents the deposition rate of
- 348  $^{234}$ Th from the bottom water. The deposition flux of  $^{234}$ Th ( $P_{Th}$ ) at the sediment-water interface can
- be calculated from the <sup>234</sup>Th<sub>ex</sub> inventory by integrating the excess <sup>234</sup>Th, namely

350 
$$P_{Th} = \int_0^Z p_{Th} dz = \lambda_{234} \cdot \int_0^Z (234Th - 238U) dz$$
 (2)

- where  $(^{234}\text{Th}-^{238}\text{U})$  is the  $^{234}\text{Th}_{ex}$  in the sediment and Z represents the extinction depth of  $^{234}\text{Th}_{ex}$ .
- The integral depth, the inventory of  $^{234}$ Th<sub>ex</sub> and the flux are shown in Table 1. Except where excess
- 353 <sup>234</sup>Th was insignificant (Stations 8 and 10), the <sup>234</sup>Th<sub>ex</sub> inventories were comparable with those
- previously determined near Fram Strait (Rutgers van der Loeff et al., 2002).
- 4.1.2 Sediment mixing rate and sedimentation rate estimated from <sup>234</sup>Th<sub>ex</sub> and <sup>228</sup>Th<sub>ex</sub>
- Once thorium isotopes are deposited to the sediment, they will continue being buried downcore
- by sedimentation. Meanwhile, sediment mixing, derived from either the disturbance due to bottom

currents or *in situ* bioturbation, also affects the Th distributions in sediments. The mixing can transport excess short-lived Th to deeper sediment where the Th<sub>ex</sub> should not otherwise be found. For example, if there was only sedimentation onto the seafloor at a given rate of 0.15 cm y<sup>-1</sup> (Hancock and Hunter, 1999), excess <sup>234</sup>Th should only be observed above ~0.075 cm. However, some excess <sup>234</sup>Th was found at the depth of 2 cm in this study. The distributions of Th<sub>ex</sub> affected by these sediment processes can be expressed with a one-dimensional steady state model using the following equation:

$$\frac{\partial T h_{ex}}{\partial t} = 0 = \frac{\partial (K \frac{\partial T h_{ex}}{\partial z})}{\partial z} - \omega \frac{\partial T h_{ex}}{\partial z} - \lambda T h_{ex}$$
(3)

where K is the sediment mixing coefficient,  $\omega$  refers to the burial rate,  $\lambda$  is the decay coefficient and Th<sub>ex</sub> refers to the activity of excess Th in the bulk sediment (dpm cm<sup>-3</sup>). The terms on the right side of Eqn. (3) represents sediment mixing, sedimentation and radioactive decay, respectively.

When it comes to  $^{234}$ Th distributions, the decay term should be significantly higher than the sedimentation term because of the high  $\lambda_{234}$  (0.0288 d<sup>-1</sup>). As a result, the sedimentation can be neglected when discussing the change of  $^{234}$ Th<sub>ex</sub> activity downcore and Eqn. (3) can be described as

$$\frac{\partial^{234} Th_{ex}}{\partial t} = \frac{\partial (K \frac{\partial^{234} Th_{ex}}{\partial z})}{\partial z} - \lambda_{234}^{234} Th_{ex}$$

$$\tag{4}$$

Assuming  $^{234}$ Th<sub>ex</sub> was in steady state and by taking the boundary conditions of  $^{234}$ Th<sub>ex</sub> =  $^{234}$ Th<sub>ex</sub> (Th activity at z = 0 cm) and  $^{234}$ Th<sub>ex</sub> = 0 below the mixing depth (i.e., the integral depth), the solution of Eqn. (4) was

377 
$$^{234}\text{Th}_{ex} = ^{234}\text{Th}_{ex0} \cdot e^{-\sqrt{\frac{\lambda}{K}}z}$$
 (5)

Thus, we calculated the mixing coefficient K from the slope of the exponential decay equation (b.

234 in Appendix Table S2,  $b_{-234} = -\sqrt{\frac{\lambda}{K}}$ ) and the results are shown in Table 2. In one case, the peak at 0.5-1 cm of Station 30 was considered to result from sediment mixing so the values of the top two layers were swapped for the regression. The <sup>234</sup>Th<sub>ex</sub> profiles at Stations 8 and 10 did not show significant <sup>234</sup>Th excess, implying that the benthic deposition was weak at these sites. Overall, the mixing coefficient shows spatial variation with the nearshore values (at Stations 16 and 21) being one order of magnitude higher than those offshore. A live sponge found in the sediment core at Station16 (Appendix Fig. S2) suggests a more active benthic environment nearshore than that in the deeper waters, supporting the highest mixing rate.

On the other hand, the decay coefficient of  $^{228}$ Th ( $\lambda_{228}$  < 0.001 d<sup>-1</sup>) is small so the sedimentation term is comparable with the decay term. The three processes affecting the rate of change in  $^{228}$ Th<sub>ex</sub> activity must be considered. As such, Eqn. (3) is expressed as:

390 
$$\frac{\partial^{228} Th_{ex}}{\partial t} = 0 = \frac{\partial (K^{\frac{\partial^{228} Th_{ex}}{\partial z}})}{\partial z} - \omega \frac{\partial^{228} Th_{ex}}{\partial z} - \lambda_{228}^{228} Th_{ex}$$
 (6)

where K is the mixing rate derived from  $^{234}$ Th<sub>ex</sub> and  $\lambda_{228}$  is the decay coefficient of  $^{228}$ Th (0.363 y<sup>-</sup> 392  $^{1}$ ). In the case of boundary conditions of  $^{228}$ Th<sub>ex</sub> =  $^{228}$ Th<sub>ex0</sub> at z=0 (Hancock and Hunter, 1999), the solution to Eqn. (6) is approximated by

394 
$${}^{228}\text{Th}_{ex} = {}^{228}\text{Th}_{ex0} \cdot e^{\frac{\omega - \sqrt{\omega^2 + 4\lambda_{228}K}}{2K}}$$
 (7)

As  $^{228}$ Th<sub>ex</sub> also exhibited an exponential decreasing trend with depth, a dynamic fitting of exponential decay was applied between  $^{228}$ Th<sub>ex</sub> and depth z. The decay parameter b<sub>-228</sub> of the regression (Appendix Table S2) was the exponential coefficient, i.e.  $b_{-228} = \frac{\omega - \sqrt{\omega^2 + 4\lambda_{228}K}}{2K}$ . The sedimentation rate can then be calculated as  $\omega = K \cdot b_{-228} - \frac{\lambda_{228}}{b_{-228}}$ . Since the sediment mixing works in the same way on  $^{234}$ Th<sub>ex</sub> and  $^{228}$ Th<sub>ex</sub>, K estimated from  $^{234}$ Th<sub>ex</sub> can be directly substituted to calculate  $\omega$ . The results are shown in Table 2. Overall, Station 21 presents the highest sedimentation rate, followed by the ridge stations (Stations 15 & 16). The sediment accumulation on the shelf break was lower by a factor of 10, a rate of <0.3 cm y<sup>-1</sup>. However, the fitting bias and the uncertainty of K led to the errors of  $\omega$  up to 100%, discouraging a budget assessment in the following discussion.

In the open ocean, excess  $^{228}$ Th in sediments is sourced from its scavenging from water column (Cochran and Masqué, 2003). We used here a constant rate of supply model (CRS) on the  $^{228}$ Th<sub>ex</sub> to derive a second estimate of sedimentation rate (Appleby and Oldfieldz, 1983). Based on this model, the sediment mixing can be regarded as an internal process with no influence on the budget of  $^{228}$ Th<sub>ex</sub>. If we assume that the total inventory of  $^{228}$ Th<sub>ex</sub> in the sediment ( $I_{228}$ ) is consistent with time, the supply of  $^{228}$ Th<sub>ex</sub> from the sedimentation should balance the decay, namely

$$\frac{\partial I_{228}}{\partial t} = 0 = R_{228} - \lambda_{228} I_{228} \tag{7}$$

where R<sub>228</sub> is the burial flux of <sup>228</sup>Th<sub>ex</sub> in the sediment after the deposition. The total inventory was calculated by trapezoidal integration from the sediment-water interface down to the depth of <sup>228</sup>Th<sub>ex</sub> extinction. As the CRS model assumes a constant supply rate, the mass accumulation flux (m) can then be estimated from the burial flux and the <sup>228</sup>Th<sub>ex</sub> activity of the top sediment layer (<sup>228</sup>Th<sub>ex</sub> at z = 0.5 cm) with  $m = R_{228}$ /<sup>228</sup>Th<sub>ex</sub>. The results are shown in Table 2. Hence, the sedimentation rate can be estimated from the mass accumulation flux divided by the dry bulk sediment density as  $\omega^* = m/(\rho \phi)$  (Andersen, 2017), which yielded a range of 0.14 ~ 0.23 cm y<sup>-1</sup> ( $\omega^*$  in Table 2). In consideration of the uncertainties, the sedimentation rates from both methods are less than 0.5 cm y<sup>-1</sup>, reasonable for a continental margin of the Northern Atlantic (Berner, 1980; Carvalho and Ramos, 1990).

# 4.2 Mercury behavior at the sediment-water interface

On the basis of half-lives and the above estimates, <sup>234</sup>Th<sub>ex</sub> was used to trace the particle deposition to the sediment-water interface; and <sup>228</sup>Th<sub>ex</sub>, with the longer half-life, was appropriate to quantify the benthic burial below the interface. As thorium and mercury species are both

particle-reactive substances, we use both Th isotopes to trace the behavior of mercury species

428 throughout shallow sediments in this section.

4.2.1 Mercury deposition and burial

450

451

452

453

454

455 456

457 458

459

460

461

462

The deposition fluxes of mercury species to the sediment can be estimated from the ratios of mercury species and <sup>234</sup>Th<sub>ex</sub> of SPM as

432 
$$P_{Hg} = P_{Th} \cdot (\frac{Hg}{2^{34}Th_{ex}})_{SPM}$$
 (8)

where  $P_{Th}$  is the deposition flux of <sup>234</sup>Th estimated in section 4.1.1. As the sediment <sup>234</sup>Th<sub>ex</sub> was 433 sourced from the dissolved  $^{234}$ Th in the bottom water,  $P_{Hg}$  refers to the mercury scavenged from 434 the bottom water to the sediment. The ratios and results are shown in Table 3. The variation of 435 mercury deposition fluxes at different stations is primarily driven by  $(\frac{Hg}{2^{34}Th_{ex}})_{SPM}$ . For MeHg, the 436 highest flux was found at Station 15 (30.6  $\pm$  6.0 pmol m<sup>-2</sup> d<sup>-1</sup>), 5 ~ 10 times higher than other sites 437  $(3.10 \sim 7.09 \text{ pmol m}^{-2} \text{ d}^{-1})$ . Differently, Station 16 had the highest deposition flux of total Hg (3100 438  $\pm$  458 pmol m<sup>-2</sup> d<sup>-1</sup>) while Station 21 had the lowest (266  $\pm$  50 pmol m<sup>-2</sup> d<sup>-1</sup>) although they are both 439 nearshore sites. One reason is that the SPM of Station 21 showed the lowest concentrations of Hg 440 species. Owing to the proximity of Scoresby Sound, part of the SPM was likely derived from 441 glacial till that has been exposed to sunlight. Photodecomposition may change the organic 442 compounds of the precipitating particles, leading to the surface sediment being less adsorptive to 443 Hg compared with marine biogenetic particles due to the lack of Hg-binding ligands (Zhang et al., 444 2019). 445

As sediment burial in this study was constrained below the interface, the concentrations of mercury species and  $^{228}$ Th<sub>ex</sub> in the top sediment were used in estimating the Hg burial flux ( $R_{Hg}$ ). With the  $^{228}$ Th<sub>ex</sub> burial flux ( $R_{228}$ ),  $R_{Hg}$  was therefore calculated with

$$R_{Hg} = R_{228} \cdot \frac{Hg}{^{228}Th_{exo}} \tag{9}$$

where  $\frac{Hg}{228Th_{ex0}}$  represents the ratio of mercury species and  $^{228}$ Th<sub>ex</sub> of 0-1 cm sediment. The related parameters and results are also shown in Table 3. For comparison, the deposition and burial fluxes of Hg species are depicted in Fig. 4. Notably, the burial fluxes of both MeHg and total Hg were higher than the deposition fluxes at Station 21. Such pattern can be attributed to the different timescales  $^{228}$ Th and  $^{234}$ Th represent. Owing to the longer half-life, part of the  $^{228}$ Th<sub>ex</sub> in the sediment can be sourced from the upper water or by lateral transport. Hence, the burial flux of Hg derived from  $R_{228}$  included inputs other than benthic scavenging. The continental detritus from the fjord area likely contributed to the high Hg burial at Station 21. Station 15 is located on the shelf of East Greenland where the overflow of EGC slows down because the EGC converged to the sill (Lin et al., 2020). Particles brought with the overflow probably precipitated on the shelf, accounting for the higher total Hg burial compared with the deposition flux.

In contrast, total Hg demonstrates significant higher deposition fluxes than burial fluxes at Stations 16 and 30 (Fig. 4), suggesting that some deposited total Hg was migrated away from the

sediment. Generally, total Hg is dominated by Hg<sup>II</sup>, which is highly particle-reactive (Heyes et al., 2004), so the total Hg should be retained in the solid phase. However, owing to the different time scales that <sup>234</sup>Th<sub>ex</sub> and <sup>228</sup>Th<sub>ex</sub> represent, the burial flux reflects a timescale of 1~10 years, during which the behavior of total Hg was not conservative. As to core top waters, the particulate total Hg concentration was linearly correlated with the TOC concentration (Appendix Fig. S3), suggesting that TOC may influence the Hg distribution. Stations 16 and 30 presented decreasing TOC profiles downcore (see Appendix Table S3), suggesting that the sediment TOC yielded to degradation with time. Correspondingly, some of total Hg was likely released from the sediment with the TOC decomposition.

Meanwhile, only a small portion of the deposited MeHg was buried into the sediment at Stations 15 and 16 (12% and 24%, respectively). Considering one aspect, MeHg was concentrated in SPM, leading to a high deposition flux (P<sub>MeHg</sub>); but, on the other hand, MeHg was not conservative in the sediment on a timescale of several years. Specifically, MeHg did not exhibit a linear relationship with TOC (middle panel of Appendix Fig. S3) so the loss mechanism should differentiate from that of total Hg. As significant concentration gradients of dissolved MeHg were shown at the sediment-water interface (Appendix Fig. S1), some MeHg might be released back into the water by diffusion and advection. Alternatively, at Stations 15 and 16, the concentrations of particle MeHg decreased downcore in the 0-3 cm sediment section, inconsistent with the changing trends of total Hg (Fig. 3), suggesting that some MeHg could be degraded within the sediment by microbial or other demethylation pathways (Benoit et al., 2003, Du et al., 2019).

The burial fluxes of total Hg were estimated in the range of 780 ~ 1890 pmol m<sup>-2</sup> d<sup>-1</sup>, higher by a factor of 3 ~ 5 than the particulate Hg export flux from the eutrophic zone (the upper 100 m) on the outer shelf of the Barents Sea (Tesán Onrubia et al., 2020). This difference suggests that the majority of Hg of the shelf sediment was sourced from benthic scavenging, and subsequently buried in the sediment. According to the distribution of dissolved manganese (Mn) in seawater (Appendix Fig. S4), small Mn plumes appeared at the bottom of trough sites (e.g., Station 13), indicating Mn was being released from the sediment. The EGC brought oxic water southward so the released Mn was likely oxidized and returned to the sediment as particulate Mn oxides, which could adsorb other metals including Ra, Th and Hg. This provides a rationale for why excess <sup>234</sup>Th, <sup>228</sup>Th, and Hg deposition were observed at the shelf stations. The difference remaining between the deposition and the burial fluxes is discussed in the next section.

## 4.2.2 Hg efflux at the sediment-water interface

Initially, we had planned to use the approach of <sup>224</sup>Ra-<sup>228</sup>Th disequilibria (Cai et al., 2012) to estimate the interfacial exchange of dissolved Hg. Unfortunately, only Stations 8 and 10 showed significant <sup>224</sup>Ra deficits in the shallow sediment. At stations where excess Th were significant, <sup>224</sup>Ra was in equilibrium with its parent <sup>228</sup>Th (Stations15 and 16 even had excess <sup>224</sup>Ra). Therefore, we use a diffusional model to provide a minimum of the efflux of dissolved mercury. With Fick's first law (Berner, 1980), fluxes driven by molecular diffusion (F<sub>M</sub>) and sediment mixing (F<sub>K</sub>) can be calculated from

$$F_{M} = \phi D_{S}^{Hg} \cdot (\frac{\partial Hg}{\partial z})_{z=0} ; F_{K} = \phi K \cdot (\frac{\partial Hg}{\partial z})_{z=0}$$
(10)

where  $\phi$  is sediment porosity calculated from the water content (Appendix Table S1), K is the sediment mixing coefficient estimated from <sup>234</sup>Th<sub>ex</sub> in section 4.1.2, and  $(\frac{\partial Hg}{\partial z})_{z=0}$  is the concentration gradient of dissolved mercury species at the sediment-water interface. The efflux of dissolved Hg species was the sum of F<sub>M</sub> and F<sub>K</sub> and the results are shown in the last two columns of Table 4.

The MeHg efflux was in a range of  $0.43 \sim 4.70 \text{ pmol m}^{-2} \text{ d}^{-1}$ . The effluxes at Stations 16/17/30were also comparable with the magnitude of the difference between the deposition and burial fluxes of MeHg (L<sub>MeHg</sub>), demonstrating that some MeHg was migrated away from the sediment by diffusion. The MeHg degradation in the sediment may account for the big difference at Station 15. In contrast, the benthic efflux of total Hg ranged between 32 and 220 pmol m<sup>-2</sup> d<sup>-1</sup> and these effluxes can only explain 2 ~ 40% of the difference between the deposition and burial fluxes of total Hg (L<sub>THg</sub>) of Stations 16/17/30, suggesting that not all of the total Hg was removed from sediment by porewater diffusion. The highest L<sub>THg</sub> was found at Stations 30 where the highest TOC was present in the top sediment. Some total Hg might be released from the sediment with the TOC decomposition, probably in forms of suspended particles or decomposed/colloidal organic matter (Schartup et al., 2014) which was then entrained by the benthic overflows southward (e.g., Station 17, see Appendix Fig. S5). Influenced by the shallowing shelf, these suspended particles would tend to redeposit when the overflow slowed down on the sill top, adding the migrated total Hg to the sediment there. This mechanism provides a manner of lateral transport, explaining the higher burial flux of total Hg at Station 15. Similarly, the released MeHg could also be transported with the overflows and deposited on the sill top (see right panel of Appendix Fig. S3), matching the highest MeHg deposition flux at Station 15. However, most MeHg (~90%) was not retained in the sediment. The lost MeHg from the sediment of the sill top may account for the MeHg hotspot observed in the mid-depth water on the downstream side of the sill (Appendix Fig. S5, unpublished data). Alternatively, the deposited Hg on the sill slope potentially increased bioavailable reactant for Hg methylation in the sediment and the resultant enhancement of MeHg in porewater, probably accounting for the MeHg hotspot near the seafloor (Appendix Fig. S5).

Overall, according to the Hg concentrations in sediments (Appendix Table S3), the sediment partition coefficient of MeHg was lower than total Hg, as found by others (Hollweg et al., 2009), resulting in more mobility of MeHg within the study area. The sediment efflux was the dominant mechanism for MeHg transport away from the sediment and would be a potential contributor of MeHg to the Irminger Sea. In contrast, the interfacial efflux played a minor role in the on-site removal for total Hg. The patterns of L<sub>THg</sub> and the unfiltered Hg of the water column indicated a benthic Hg redistribution on the upstream side of the sill and most was retained on the shallow shelf sediment. Given the different behaviors of MeHg and total Hg at the sediment-water interface, benthic efflux was consciously considered in estimating the benthic Hg scavenging.

### 4.3 Benthic Hg scavenging in the high-latitude North Atlantic

In earlier studies of the Hg budget between the North Atlantic and Arctic Oceans, the total Hg fluxes along the EGC were reported to be decreasing from 54 Mg y<sup>-1</sup> (transect ①) across the Fram Strait (one of the Arctic gateways) to 45 Mg y<sup>-1</sup> when passing 60°N (transect ③) (Cossa et al.,

2018; Petrova et al., 2020). On the east side, the total Hg flux along NAC declined from 64 Mg y (transect ③) to 49 ± 10 Mg y (transects ①) and ②) at the Arctic gateway around Spitsbergen Islands (left panel of Fig. 1). In total, the Hg loss in the high-latitude North Atlantic regions (60 ~ 80°N) was ~24 Mg y \cdot . According to the estimates on the Hg deposition and burial fluxes as well as the efflux at the sediment-water interface (section 4.2), the sediment in the study area could be regarded as a Hg sink for the bottom overflows from the Arctic Ocean to the North Atlantic Ocean. The average Hg fluxes of Stations 15/16/17/30 were used to estimate the benthic scavenging considering that Stations 8/10/36 did not show excess Th in the sediment and Station 21 was affected by the continental inputs. Scavenging areas were framed on the shallow shelf-sill zones of Greenland-Iceland-Faroes Islands ridge, marked by the orange trapezoids in the right panel of Fig. 1 which represent the upstream region between 65.2 ~ 67.5°N, covering Stations 15/16/17, and the east coast of the Faroes bank, covering Station 30. These areas are 1.0×10<sup>5</sup> km² in total. We did not extend the area to the whole shelf of the high-latitude North Atlantic in case this led to an overestimation on the benthic scavenging.

For total Hg, the deposited portion was mostly retained in the sediment even though some might be laterally transported to the sill top with the overflows, so the average deposition flux of Stations  $15/16/17/30~(2024~\pm~960~\text{pmol}~\text{m}^{-2}~\text{d}^{-1})$  was applied. Using this value, the annual benthic scavenging on total Hg was estimated to be  $14.8~\pm~7.0~\text{Mg}~\text{y}^{-1}$ , accounting for over half of the previously estimated Hg loss (~24 Mg y<sup>-1</sup>) in the high-latitude North Atlantic Ocean. This calculation suggests that the benthic processes on the shallow sills lessened the Hg export from the Arctic Ocean to the Atlantic Ocean. Notably, our study only estimated the sediment scavenging on the shallow sills around Iceland due to the limitation of sampling sites. Such scavenging might also occur on other shallow ridges or plateaus like Iceland-Faroes Ridge and Yermak Plateau, potentially accounting for the other half of previously estimated Hg loss.

Given that a portion of the deposited MeHg diffused away from the sediment and was then transported southward with overflows, the MeHg scavenging was quantified with the average burial flux of Stations 15/16/17/30 ( $3.43 \pm 1.21$  pmol m<sup>-2</sup> d<sup>-1</sup>). Accordingly, the annual rate was estimated to be  $27 \pm 10$  kg y<sup>-1</sup>. Compared with the previously estimated MeHg export from the Arctic Ocean via the Fram Strait ( $6 \pm 2$  Mg y<sup>-1</sup>, Petrova et al., 2020), the benthic scavenging in our study area was almost negligible. However, the bottom MeHg concentration along the Fram Strait transect ( $0.2 \sim 0.4$  pmol L<sup>-1</sup>, Petrova et al. 2020) is generally higher than that along Greenland-Iceland ridge ( $0.05 \sim 0.25$  pmol L<sup>-1</sup>, our unpublished data), implying that temporary MeHg scavenging could have occurred on the shallow shelf, leading to the decrease in MeHg concentration in the bottom water. Overall, the MeHg was not permanently buried in the sediment. Most could leave the sediment as dissolved MeHg via diffusion and advection. The shelf sediment was therefore more like a buffer zone where MeHg from the polar waters was retarded on a short timescale (days to months) and was slowly released to the water column on a long timescale (months to years).

In summary, the deposited total Hg we quantified with <sup>234</sup>Th<sub>ex</sub> was approximately similar to the portion scavenged from water column in the high-latitude North Atlantic. For MeHg, only the buried part maintained in the sediment accounted for the MeHg loss of the water column. The

behavior of Hg species at the bottom boundary and the related processes are detailed and outlined in Fig. 5. With the influence of overflows, both MeHg and total Hg were deposited by the suspended particles onto the surface sediment. Owing to their different properties, a fraction of MeHg diffused to the water column as dissolved phase so ~50% of the deposited MeHg was buried in the sediment; while only a minor fraction of the total Hg was released to the water column by diffusion and another portion was migrated to the water column as particulate Hg, which was finally deposited and buried into sediment when the flows met with the sills and slowed down while passing the slope regions. On the other side of the ridge, the bottom flow passing the sill is intense, stimulating benthic exchange to replenish MeHg and enhance its transport towards the Irminger Sea.

## 5. Conclusion

In this study, we used two short-lived Th isotopes to investigate the dynamic benthic processes of sediment deposition and burial, and to quantify the benthic scavenging rate of MeHg and total Hg around Iceland. The sediment <sup>234</sup>Th<sub>ex</sub> was utilized to estimate the deposition flux and <sup>228</sup>Th<sub>ex</sub> was used to estimate the benthic burial flux. Our study showed that benthic scavenging mainly occurred on the shallow shelves where water depth is less than 800 m. The resuspended particles scavenged  $27 \pm 10 \text{ kg y}^{-1}$  of MeHg and  $14.8 \pm 7.0 \text{ Mg y}^{-1}$  of total Hg from bottom water to the sediment. Owing to the different geochemical behaviors, most of the deposited total Hg was retained in sediment, but <50% of the MeHg was buried. The "missing" MeHg was inferred to be released to the water column through interfacial diffusion and advection and that it continued being transported over the sill with the overflow water. Furthermore, the estimated benthic Hg scavenging on the shallow shelves and sill regions explained >50% of the previously reported Hg loss between the Arctic and Atlantic Oceans, indicating that the shelf/sill sediment is a main Hg sink in the high-latitude North Atlantic (60-70 °N) and that there may not be net transport of Hg from the Arctic to the North Atlantic Ocean on a timescale of decades. Hence, the shallow shelves and sills acted as a buffer zone for the polar overflow waters, retarding the movement of particulate-active inorganic Hg species to the North Atlantic deep waters. According to the different timescales of these benthic processes, some Hg species tended to migrate away from the sediment on a longer timescale. The biogeochemical cycling of organic compounds likely influenced the interfacial exchange of Hg species, considering the good correlation between TOC and particulate total Hg. Our study implies that more Hg could be imported to the deep waters of North Atlantic in the future if more organic matter in sediment becomes labile with climate-driven increases in water temperature.

### Acknowledgements

This study was funded by USA National Science Foundation (NSF 2123575) and National Science Foundation of China (NSFC 42206042) and the expedition aboard Pelagia (PE64-474) was funded by the Dutch Research Council (NWO; grant 016.Vidi.189.138 to R. Middag). The lab work was completed during the time XS worked as a postdoctoral investigator in the

624	Department of Marine Sciences at the University of Connecticut (UConn). Partial support for the
625	research came from a NERC fellowship (NE/P017630/1) to AA. The authors thank Katsiaryna
626	Pabortsava for her help with the first <sup>234</sup> Th counting in NOC, and thank Steve Pike, Ken Buessele
627	and Peigen Lin for the second counting at WHOI. XS expresses gratitude to the crew and scientists
628	on RV Pelagia for their help on sampling and to Pinghe Cai for his advice on flux calculations
629	Claudia Koerting, Lingjie Lin and Yiping He assisted with the TOC and TN measurement.
630	
631	CRediT authorship contribution statement
632	Xiangming Shi: Writing - Original Draft, Conceptualization, Methodology, Data curation
633	Formal analysis, Writing- Reviewing and Editing, Funding acquisition. Amber L. Annett
634	Investigation, Resources, Data Curation, Funding acquisition, Writing- Reviewing and Editing
635	Rhiannon L. C. Jones: Investigation, Project administration, Writing- Reviewing and Editing. Rol
636	Middag: Investigation, Funding acquisition, Writing- Reviewing and Editing. Robert P. Mason
637	Conceptualization, Resources, Funding acquisition, Writing- Reviewing and Editing, Supervision
638	
639	Data availability
640	Data are available through Mendeley Data at <a href="https://data.mendeley.com/drafts/6hgydz2fm8">https://data.mendeley.com/drafts/6hgydz2fm8</a> .
641	
642	Appendix A. Supplementary Material

Supplementary material, appendix tables and figures, to this article can be found online.

661

662

663 664

665 666

667

668

669 670

671

672

673

674

675

679

680

684

685

- Agather, A.M., Bowman, K.L., Lamborg, C.H. and Hammerschmidt, C.R. (2017) Distribution of mercury species in the western Arctic Ocean, ASLO, Honolulu, HI.
- Amos, H.M., Jacob, D.J., Streets, D.G. and Sunderland, E.M. (2013) Legacy impacts of all-time anthropogenic emissions on the global mercury cycle. Global Biogeochemical Cycles 27, 410-421.
- Andersen, T.J. (2017) Some Practical Considerations Regarding the Application of 210Pb and 137Cs
  Dating to Estuarine Sediments, in: Weckström, K., Saunders, K.M., Gell, P.A., Skilbeck, C.G. (Eds.),
  Applications of Paleoenvironmental Techniques in Estuarine Studies. Springer Netherlands, Dordrecht,
  pp. 121-140.
- Appleby, P.G. and Oldfieldz, F. (1983) The assessment of 210Pb data from sites with varying sediment accumulation rates. Hydrobiologia 103, 29-35.
- Araujo, B.F., Osterwalder, S., Szponar, N., Lee, D., Petrova, M.V., Pernov, J.B., Ahmed, S., Heimbürger-Boavida, L.-E., Laffont, L., Teisserenc, R., Tananaev, N., Nordstrom, C., Magand, O., Stupple, G.,
   Skov, H., Steffen, A., Bergquist, B., Pfaffhuber, K.A., Thomas, J.L., Scheper, S., Petäjä, T.,
   Dommergue, A. and Sonke, J.E. (2022) Mercury isotope evidence for Arctic summertime re-emission of mercury from the cryosphere. Nature communications 13, 4956.
  - Balcom, P.H., Hammerschmidt, C.R., Fitzgerald, W.F., Lamborg, C.H. and O'Connor, J.S. (2008) Seasonal distributions and cycling of mercury and methylmercury in the waters of New York/New Jersey Harbor Estuary. Marine Chemistry 109, 1-17.
  - Beaird, N.L., Rhines, P.B. and Eriksen, C.C. (2013) Overflow Waters at the Iceland–Faroe Ridge Observed in Multiyear Seaglider Surveys. Journal of Physical Oceanography 43, 2334-2351.
  - Benoit, J. M., Gilmour, C. C., Heyes, A., Mason, R. P. and Miller, C. L. (2003) Geochemical and Biological Controls Over Methylmercury Production and Degradation in Aquatic Ecosystems. ACS Symposium Series, pp. 262-297.
  - Berner, R.A. (1980) Early Diagenesis-A Theoretical Approach, in: Princeton (Ed.). Princeton University Press, New Jersey, p. 334.
  - Bloom, N. (1989) Determination of picogram levels of methylmercury by aqueous phase ethylation, followed by cryogenic gas chromatography with cold vapour atomic fluorescence detection. Canadian Journal of Fisheries and Aquatic Sciences 46, 1131-1140.
  - Bowman, K.L., Hammerschmidt, C.R., Lamborg, C.H. and Swarr, G. (2015) Mercury in the North Atlantic Ocean: The U.S. GEOTRACES zonal and meridional sections. Deep Sea Research Part II: Topical Studies in Oceanography 116, 251-261.
- Cai, P., Shi, X., Hong, Q., Li, Q., Liu, L., Guo, X. and Dai, M. (2015) Using <sup>224</sup>Ra/<sup>228</sup>Th disequilibrium to quantify benthic fluxes of dissolved inorganic carbon and nutrients into the Pearl River Estuary.
   Geochim. Cosmochim. Acta 170, 188-203.
  - Cai, P., Shi, X., Moore, W.S. and Dai, M. (2012) Measurement of <sup>224</sup>Ra:<sup>228</sup>Th disequilibrium in coastal sediments using a delayed coincidence counter. Marine Chemistry 138-139, 1-6.
- Cai, P., Shi, X., Moore, W.S., Peng, S., Wang, G. and Dai, M. (2014) <sup>224</sup>Ra:<sup>228</sup>Th disequilibrium in coastal sediments: Implications for solute transfer across the sediment–water interface. Geochimica et Cosmochimica Acta 125, 68-84.
  - Carvalho, F.P. and Ramos, L.A. (1990) Lead-210 chronology in marine sediments from the northern continental margin of Portugal, Proceedings of the Second National Conference on Environmental Quality. Lisbon Universidade Nova de Lisboa, pp. 143-151.
- Coale, K.H. and Bruland, K.W. (1987) Oceanic stratified euphotic zone as elucidated by 234Th: 238U disequilibria1. Limnology and Oceanography 32, 189-200.
- Cochran, J.K. and Masqué, P. (2003) Short-lived U/Th Series Radionuclides in the Ocean: Tracers for
   Scavenging Rates, Export Fluxes and Particle Dynamics. Reviews in Mineralogy and Geochemistry
   52, 461-492.
- Cossa, D., Heimbürger, L.E., Pérez, F.F., García-Ibáñez, M.I., Sonke, J.E., Planquette, H., Lherminier, P.,
   Boutorh, J., Cheize, M., Menzel Barraqueta, J.L., Shelley, R. and Sarthou, G. (2018) Mercury

- distribution and transport in the North Atlantic Ocean along the GEOTRACES-GA01 transect. Biogeosciences 15, 2309-2323.
- Dastoor, A., Angot, H., Bieser, J., Christensen, J.H., Douglas, T.A., Heimbürger-Boavida, L.-E., Jiskra, M.,
   Mason, R.P., McLagan, D.S., Obrist, D., Outridge, P.M., Petrova, M.V., Ryjkov, A., St. Pierre, K.A.,
   Schartup, A.T., Soerensen, A.L., Toyota, K., Travnikov, O., Wilson, S.J. and Zdanowicz, C. (2022)
   Arctic mercury cycling. Nature Reviews Earth & Environment 3, 270-286.

702

703

708

709

- Davidson, P.W., Palumbo, D., Myers, G.J., Cox, C., Shamlaye, C.F., Sloane-Reeves, J., Cernichiari, E., Wilding, G.E. and Clarkson, T.W. (2000) Neurodevelopmental Outcomes of Seychellois Children from the Pilot Cohort at 108 Months Following Prenatal Exposure to Methylmercury from a Maternal Fish Diet. Environmental Research 84, 1-11.
- Dickson, R.R. and Brown, J. (1994) The production of North Atlantic Deep Water: Sources, rates, and pathways. Journal of Geophysical Research: Oceans 99, 12319-12341.
- Dietz, R., Outridge, P.M. and Hobson, K.A. (2009) Anthropogenic contributions to mercury levels in present-day Arctic animals—A review. Science of The Total Environment 407, 6120-6131.
  - DiMento, B.P., Mason, R.P., Brooks, S. and Moore, C. (2019) The impact of sea ice on the air-sea exchange of mercury in the Arctic Ocean. Deep Sea Research Part I: Oceanographic Research Papers 144, 28-38.
- Driscoll, C.T., Mason, R.P., Chan, H.M., Jacob, D.J. and Pirrone, N. (2013) Mercury as a global pollutant:
   sources, pathways, and effects. Environmental Science & Technology 47, 4967-4983.
- Du, H., Ma, M., Igarashi, Y. and Wang, D. (2019) Biotic and Abiotic Degradation of Methylmercury in Aquatic Ecosystems: A Review. Bulletin of Environmental Contamination and Toxicology 102, 605-611.
- EPA, U. (2001) Methyl Mercury in Water by Distillation, Aqueous Ethylation, Purge and Trap, and Cold
   Vapor Atomic Fluorescence Spectrometry), Method 1630, Washington DC.
- Foukal, N. P., Gelderloos, R., Pickart, R. S. (2020) A continuous pathway for fresh water along the East Greenland shelf. Science Advance 6, eabc4254.
- Grandjean, P., Weihe, P., White, R.F., Debes, F., Araki, S., Yokoyama, K., Murata, K., SØRensen, N.,
   Dahl, R. and JØRgensen, P.J. (1997) Cognitive Deficit in 7-Year-Old Children with Prenatal Exposure
   to Methylmercury. Neurotoxicology and Teratology 19, 417-428.
- Gardner, W., Richardson, M.J., Mishonov, A.V. and Biscaye, P.E. (2018) Global comparison of benthic nepheloid layers based on 52 years of nephelometer and transmissometer measurements. Progress in Oceanography.
- Hammerschmidt, C.R. and Fitzgerald, W.F. (2006) Methylmercury cycling in sediments on the continental shelf of southern New England. Geochimica et Cosmochimica Acta 70, 918-930.
- Hancock, G.J. and Hunter, J.R. (1999) Use of excess <sup>210</sup>Pb and <sup>228</sup>Th to estimate rates of sediment accumulation and bioturbation in Port Phillip Bay, Australia. Marine and Freshwater Research 50, 533-545.
- Hansen, B. and Østerhus, S. (2000) North Atlantic–Nordic Seas exchanges. Progress in Oceanography 45, 109-208.
- Hansen, B., Østerhus, S., Hátún, H., Kristiansen, R. and Larsen, K.M.H. (2003) The Iceland-Faroe inflow of Atlantic water to the Nordic Seas. Progress in Oceanography 59, 443-474.
- Hasholt, B., Nielsen, T.F., Mankoff, K.D., Gkinis, V. and Overeem, I. (2022) Sediment concentrations and transport in icebergs, Scoresby Sound, East Greenland. Hydrological Processes 36, e14668.
- Hawkings, J.R., Linhoff, B.S., Wadham, J.L., Stibal, M., Lamborg, C.H., Carling, G.T., Lamarche-Gagnon, G., Kohler, T.J., Ward, R., Hendry, K.R., Falteisek, L., Kellerman, A.M., Cameron, K.A., Hatton, J.E.,
- 739 Tingey, S., Holt, A.D., Vinšová, P., Hofer, S., Bulínová, M., Větrovský, T., Meire, L. and Spencer,
- R.G.M. (2021) Large subglacial source of mercury from the southwestern margin of the Greenland Ice Sheet. Nature Geoscience 14, 496-502.

- Hein, d.B. (2010) eGEOTRACES-GA02 Total <sup>234</sup>Th of seawater samples, in: Loes, G. (Ed.),
   https://geotraces.webodv.awi.de/IDP2021%3EGEOTRACES\_IDP2021\_Seawater\_Discrete\_Sample
   Data v1/service/DataExploration#.
- Heyes, A., Miller, C. and Mason, R. (2004) Mercury and methylmercury in Hudson River sediment: impact of tidal resuspension on partitioning and methylation. Marine Chemistry 90, 75-89.

- Hollweg, T.A., Gilmour, C.C., Mason R.P (2009) Methylmercury production in sediments of Chesapeake Bay and the mid-Atlantic continental margin. Marine Chemistry 114, 86-101.
- Hong, Q., Peng, S., Zhao, D. and Cai, P. (2021) Cross-shelf export of particulate organic carbon in the northern South China Sea: Insights from a 234Th mass balance. Progress in Oceanography 193, 102532.
- Jensen, S. and Jernelöv, A. (1969) Biological methylation of mercury in aquatic organisms. Nature 223, 753-754.
- Lamborg, C., Bowman, K., Hammerschmidt, C., Gilmour, C., Munson, K., Selin, N. and Tseng, C.-M. (2014) Mercury in the Anthropocene Ocean. Oceanography 27, 76-87.
  - Le Gland, G., Aumont, O. and Mémery, L. (2019) An Estimate of Thorium 234 Partition Coefficients Through Global Inverse Modeling. Journal of Geophysical Research: Oceans 124, 3575-3606.
  - Lin, P., Pickart, R.S., Jochumsen, K., Moore, G.W.K., Valdimarsson, H., Fristedt, T. and Pratt, L.J. (2020) Kinematic Structure and Dynamics of the Denmark Strait Overflow from Ship-Based Observations. Journal of Physical Oceanography 50, 3235-3251.
  - Mason, R.P., Rolfhus, K.R. and Fitzgerald, W.F. (1995) Methylated and elemental mercury cycling in surface and deep ocean waters of the North Atlantic. Water, Air, and Soil Pollution 80, 665-677.
  - Østerhus, S., Sherwin, T., Quadfasel, D. and Hansen, B. (2008) The Overflow Transport East of Iceland, in: Dickson, R.R., Meincke, J., Rhines, P. (Eds.), Arctic–Subarctic Ocean Fluxes: Defining the Role of the Northern Seas in Climate. Springer Netherlands, Dordrecht, pp. 427-441.
  - Overeem, I., Hudson, B.D., Syvitski, J.P.M., Mikkelsen, A.B., Hasholt, B., van den Broeke, M.R., Noël, B.P.Y. and Morlighem, M. (2017) Substantial export of suspended sediment to the global oceans from glacial erosion in Greenland. Nature Geoscience 10, 859-863.
  - Petrova, M.V., Krisch, S., Lodeiro, P., Valk, O., Dufour, A., Rijkenberg, M.J.A., Achterberg, E.P., Rabe, B., Rutgers van der Loeff, M., Hamelin, B., Sonke, J.E., Garnier, C. and Heimbürger-Boavida, L.-E. (2020) Mercury species export from the Arctic to the Atlantic Ocean. Marine Chemistry 225, 103855.
  - Puigcorbé, V., Roca-Martí, M., Masqué, P., Benitez-Nelson, C., Rutgers van der Loeff, M., Bracher, A. and Moreau, S. (2017) Latitudinal distributions of particulate carbon export across the North Western Atlantic Ocean. Deep Sea Research Part I: Oceanographic Research Papers 129, 116-130.
  - Rutgers van der Loeff, M.M., Meyer, R., Rudels, B. and Rachor, E. (2002) Resuspension and particle transport in the benthic nepheloid layer in and near Fram Strait in relation to faunal abundances and <sup>234</sup>Th depletion. Deep Sea Research Part I: Oceanographic Research Papers 49, 1941-1958.
  - Schartup, A.T., Balcom, P.H. and Mason, R.P. (2014) Sediment-porewater partitioning, total sulfur, and methylmercury production in estuaries. Environmental Science and Technology 48, 954-960.
  - Seelen, E.A., Massey, G.M. and Mason, R.P. (2018) Role of sediment resuspension on estuarine suspended particulate mercury dynamics. Environmental Science and Technology 52, 7736-7744.
- Shi, X., Mason, R.P., Charette, M.A., Mazrui, N.M. and Cai, P. (2018) Mercury flux from salt marsh sediments: Insights from a comparison between <sup>224</sup>Ra/<sup>228</sup>Th disequilibrium and core incubation methods. Geochimica et Cosmochimica Acta 222, 569-583.
- Soerensen, A.L., Jacob, D.J., Schartup, A.T., Fisher, J.A., Lehnherr, I., St Louis, V.L., Heimburger, L.E., Sonke, J.E., Krabbenhoft, D.P. and Sunderland, E.M. (2016) A mass budget for mercury and methylmercury in the Arctic Ocean. Global Biogeochemical Cycles 30, 560-575.
- Soerensen, A.L., Sunderland, E.M., Holmes, C.D., Jacob, D.J., Yantosca, R.M., Skov, H., Christensen, J.H.,
   Strode, S.A. and Mason, R.P. (2010) An improved global model for air-sea exchange of mercury: high
   concentrations over the North Atlantic. Environmental Science and Technology 44, 8574-8580.
- Sunderland, E.M. and Mason, R.P. (2007) Human impacts on open ocean mercury concentrations. Global
   Biogeochemical Cycles 21, GB4022.

- Tamborski, J.J., Cai, P., Eagle, M., Henderson, P. and Charette, M.A. (2022) Revisiting 228Th as a tool for determining sedimentation and mass accumulation rates. Chemical Geology 607, 121006.
- Tesán Onrubia, J.A., Petrova, M.V., Puigcorbé, V., Black, E.E., Valk, O., Dufour, A., Hamelin, B.,
   Buesseler, K.O., Masqué, P., Le Moigne, F.A.C., Sonke, J.E., Rutgers van der Loeff, M. and
   Heimbürger-Boavida, L.-E. (2020) Mercury export flux in the Arctic Ocean estimated from <sup>234</sup>Th/<sup>238</sup>U disequilibria. ACS Earth and Space Chemistry 4, 795-801.

800

801 802

- Xu, B., Bianchi, T.S., Allison, M.A., Dimova, N.T., Wang, H., Zhang, L., Diao, S., Jiang, X., Zhen, Y., Yao, P., Chen, H., Yao, Q., Dong, W., Sui, J. and Yu, Z. (2015) Using multi-radiotracer techniques to better understand sedimentary dynamics of reworked muds in the Changjiang River estuary and inner shelf of East China Sea. Marine Geology 370, 76-86.
- Zhang, L., Wu, S., Zhao, L., Lu, X., Pierce, E.M. and Gu, B. (2019) Mercury Sorption and Desorption on Organo-Mineral Particulates as a Source for Microbial Methylation. Environmental Science & Technology 53, 2426-2433.
- Zhang, Y., Soerensen, A.L., Schartup, A.T. and Sunderland, E.M. (2020) A global model for methylmercury formation and uptake at the base of marine food webs. Global Biogeochemical Cycles 34, e2019GB006348.

Table 1. The integral depth, the inventory in the sediment for the deposition flux of <sup>234</sup>Th<sub>ex</sub>.

Station	Latitude (°N)	Longitude (°W)	Integral depth Z (cm)	Inventory of <sup>234</sup> Th <sub>ex</sub> (dpm cm <sup>-2</sup> )*	<sup>234</sup> Th <sub>ex</sub> deposition flux (P <sub>Th</sub> , dpm m <sup>-2</sup> d <sup>-1</sup> )
Station 8	63.17	37.00	7	$-0.68 \pm 0.65$	_
Station 10	65.25	30.67	7	$-0.62 \pm 0.51$	
Station 15	66.67	28.33	2	$1.83 \pm 0.36$	$527 \pm 104$
Station 16	67.69	31.12	4	$2.39 \pm 0.35$	$689 \pm 102$
Station 17	67.50	25.83	2	$1.15 \pm 0.28$	$331 \pm 81$
Station 21	69.98	21.63	3	$1.48 \pm 0.28$	$426 \pm 80$
Station 30	61.67	3.00	2	$3.02 \pm 0.37$	$869 \pm 107$
Station 36	62.00	10.67	3	_	

<sup>\*</sup> error: 3σ.

Table 2 Sediment mixing coefficient and sedimentation rate derived from  $^{234}Th_{ex}$  and  $^{228}Th_{ex}$ , and mass accumulation rate derived from  $^{228}Th_{ex}$  only

Station	Sediment mixing coefficient K (cm <sup>2</sup> d <sup>-1</sup> )	Sedimentation rate (ω, cm y <sup>-1</sup> )	$^{228}$ Th <sub>ex</sub> burial flux (R <sub>228</sub> , dpm m <sup>-2</sup> d <sup>-1</sup> )	Mass accumulation flux (m, g cm <sup>-2</sup> y <sup>-1</sup> )	Sedimentation rate (ω*, cm y <sup>-1</sup> )
Station 15	$0.0045 \pm 0.0011$	$1.15 \pm 0.42$	$3.38 \pm 0.36$	$0.47 \pm 0.09$	$0.23 \pm 0.04$
Station 16	$0.0420 \pm 0.0150$	$27.4 \pm 28.3$	$10.0 \pm 0.38$	$0.37 \pm 0.02$	$0.16 \pm 0.01$
Station 17	$0.0010 \pm 0.0005$	$0.32 \pm 0.28$	$6.34 \pm 0.21$	$0.38 \pm 0.02$	$0.19 \pm 0.01$
Station 21	$0.0151 \pm 0.0043$	$4.60 \pm 2.00$	$5.28 \pm 0.23$	$0.30 \pm 0.02$	$0.14 \pm 0.01$
Station 30	$0.0007 \pm 0.0001$	$0.27 \pm 0.10$	$5.64 \pm 0.16$	$0.31 \pm 0.02$	$0.15 \pm 0.01$

<sup>\*:</sup> Based on the CRS model.

Table 3 Ratios of mercury species and  $^{234}$ Th<sub>ex</sub> in SPM; ratios of mercury species and  $^{228}$ Th<sub>ex</sub> in the top sediment; mercury redeposition fluxes traced by  $^{234}$ Th<sub>ex</sub>; and mercury burial rate from the top sediment traced by  $^{228}$ Th<sub>ex</sub>.

ID	$\frac{\text{MeHg}}{^{234}\text{Th}_{ex}}$ (pmol dpm $^{-1}$ )	$\frac{\text{Total Hg}}{^{234}\text{Th}_{ex}}$ (pmol dpm $^{-1}$ )	$\frac{\text{MeHg}}{^{228}\text{Th}_{ex}}$ (pmol dpm $^{-1}$ )	$\frac{\text{Total Hg}}{^{228}\text{Th}_{ex}}$ (pmol dpm $^{-1}$ )	MeHg deposition flux (pmol m <sup>-2</sup> d <sup>-1</sup> )	Total Hg deposition flux (pmol m <sup>-2</sup> d <sup>-1</sup> )	MeHg burial flux* (pmol m <sup>-2</sup> d <sup>-1</sup> )	Total Hg burial flux* (pmol m <sup>-2</sup> d <sup>-1</sup> )
Station 8	0.002	1.04	_	_	_	_	_	_
Station 10	0.002	1.84	_		_	_	_	_
Station 15	0.058	1.75	1.08	454	$30.6 \pm 6.0$	$925 \pm 182$	$3.66 \pm 0.39$	$1533 \pm 165$
Station 16	0.010	4.50	0.17	189	$7.09 \pm 1.05$	$3100 \pm 458$	$1.73 \pm 0.07$	$1891 \pm 72$
Station 17	0.017	4.83	0.59	170	$5.47 \pm 1.35$	$1600 \pm 393$	$3.73 \pm 0.12$	$1078 \pm 36$
Station 21	0.007	0.62	1.14	290	$3.10 \pm 0.58$	$266 \pm 50$	$6.04 \pm 0.26$	$1532 \pm 67$
Station 30	0.007	2.85	0.81	138	$6.05 \pm 0.75$	$2470 \pm 305$	$4.60 \pm 0.13$	$781 \pm 23$
Average#					$12.3 \pm 12.3$	$2024 \pm 960$	$3.43 \pm 1.21$	$1321 \pm 490$

<sup>\*</sup>Calculated from the accumulation rate (*m*) estimated based on <sup>228</sup>Th<sub>ex</sub> profiles and the Hg concentration in the surface sediment.

Table 4 Effluxes of mercury species based on a diffusional model.

ID	D <sub>s</sub> <sup>MeHg</sup> (10 <sup>-6</sup> cm <sup>2</sup> s <sup>-1</sup> )	$D_s^{THg}$ (10 <sup>-6</sup> cm <sup>2</sup> s <sup>-1</sup> )	$\left(\frac{\partial MeHg}{\partial z}\right)_{z=0}$ (pmol/L/cm)	$\left(\frac{\partial \text{THg}}{\partial z}\right)_{z=0}$ (pmol/L/cm)	$F_{\text{MeHg}} (F_{\text{M}} + F_{\text{K}})^{\#}$ (pmol m <sup>-2</sup> d <sup>-1</sup> )	$F_{THg} (F_M + F_K)^\#$ (pmol m <sup>-2</sup> d <sup>-1</sup> )
Station 8	3.9	2.6	1.78	29.93	4.63*	51.76*
Station 10	3.6	2.4	0.18	20.35	0.43*	31.88*
Station 15	4.0	2.6	1.14	30.73	3.13 (3.09+0.04)	56.6 (55.5+1.09)
Station 16	4.6	3.0	1.23	28.78	4.70 (4.25+0.45)	76.8 (66.2+10.6)
Station 17	3.8	2.5	1.64	127.99	4.24 (4.23+0.01)	221 (220.0+1.03)
Station 21	4.2	2.8	0.26	34.37	0.82 (0.78+0.03)	73.5 (69.1+4.34)
Station 30	3.9	2.6	0.65	19.73	1.81 (1.81+0.00)	36.9 (36.8+0.12)

<sup>\*</sup> Molecular diffusion only.

<sup>\*</sup>Average flux of Stations 15/16/17/30. The error stands for the standard deviation.

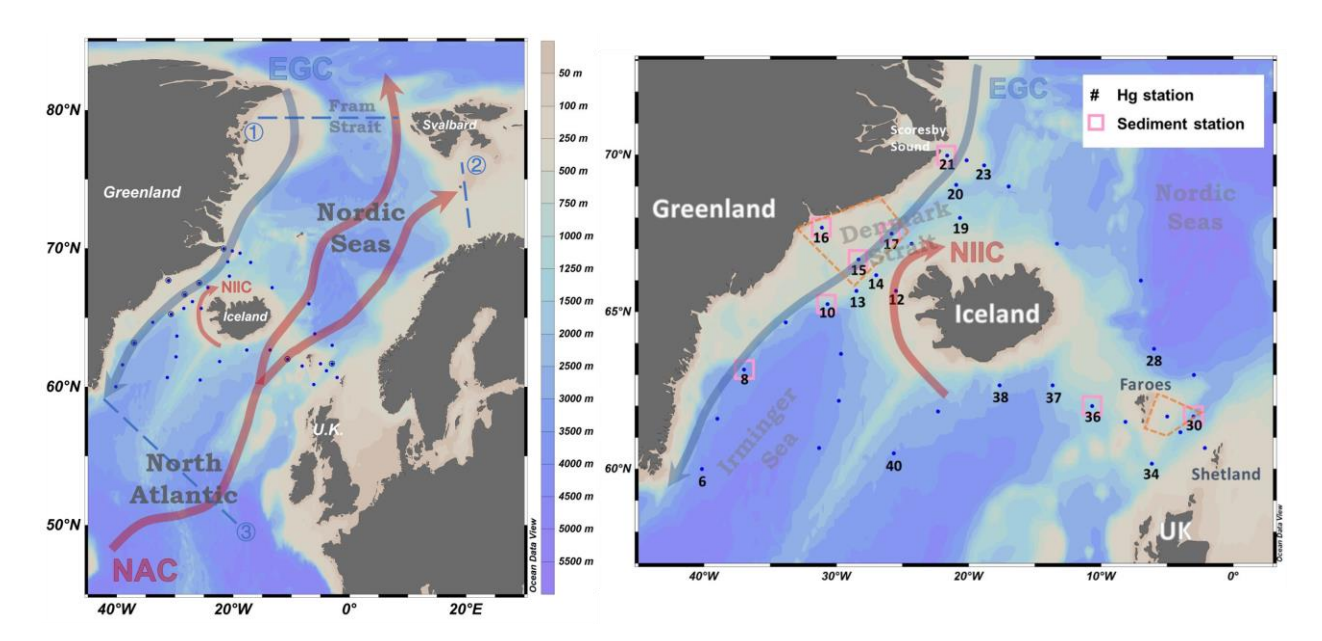


Fig. 1 Left panel: schematic of the currents around Iceland: East Greenland Current (EGC, in blue); North Icelandic Irminger Current (NIIC, in red); and North Atlantic Current (NAC, in red). According to Petrova et al. (2020), total mercury (total Hg) fluxes in EGC passing transects 1 and 3 were 54  $\pm$  13 Mg/y and ~45 Mg/y, respectively; and in NAC, the fluxes passing 3, 2 and 1 were ~64 Mg/y, 6  $\pm$  6 Mg/y and 43  $\pm$  9 Mg/y, respectively.

Right panel: sampling stations. The pink squares mark the sediment sites. The orange trapezoids refer to regions modeling Hg scavenging (see text section 4.3).

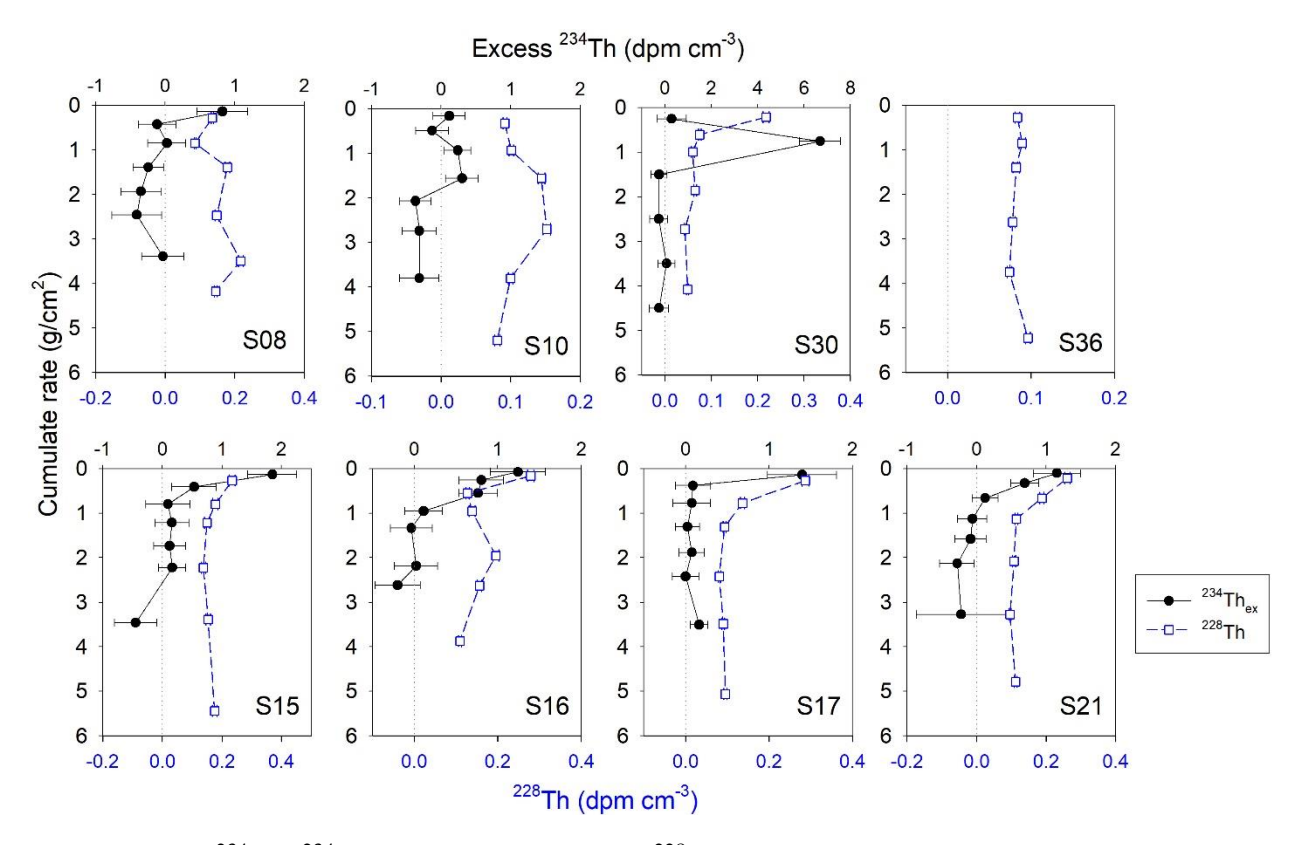


Fig.2 Excess  $^{234}$ Th ( $^{234}$ Th<sub>ex</sub>) and surface-bound  $^{228}$ Th activities in the bulk sediment. The upper panel shows stations with water depth >1000 m. The lower panel shows the stations on the Greenland shelf with a water depth range of 300-800 m.

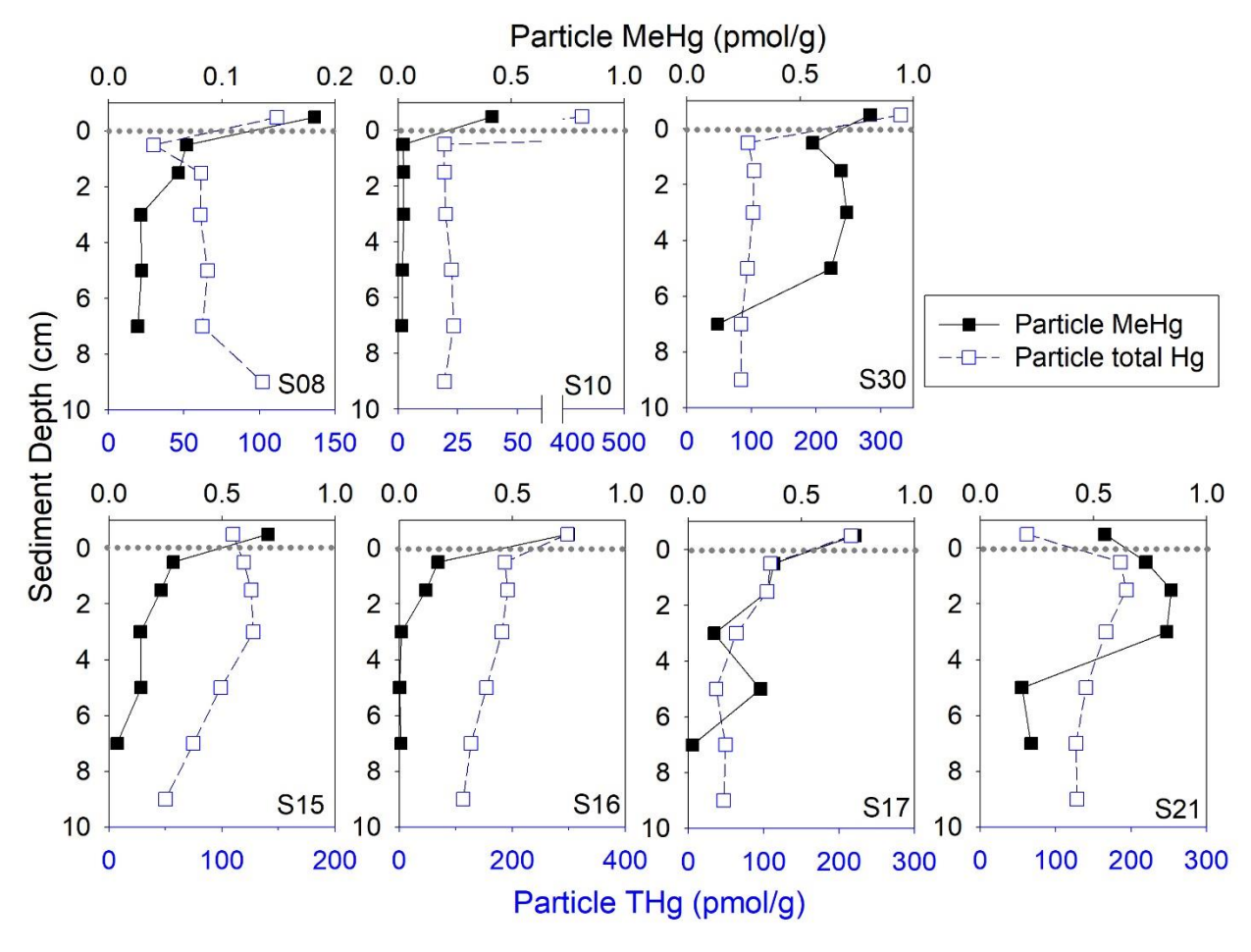


Fig.3 The distributions of methylmercury (MeHg) and total mercury (THg) in the sediment (dry weight)

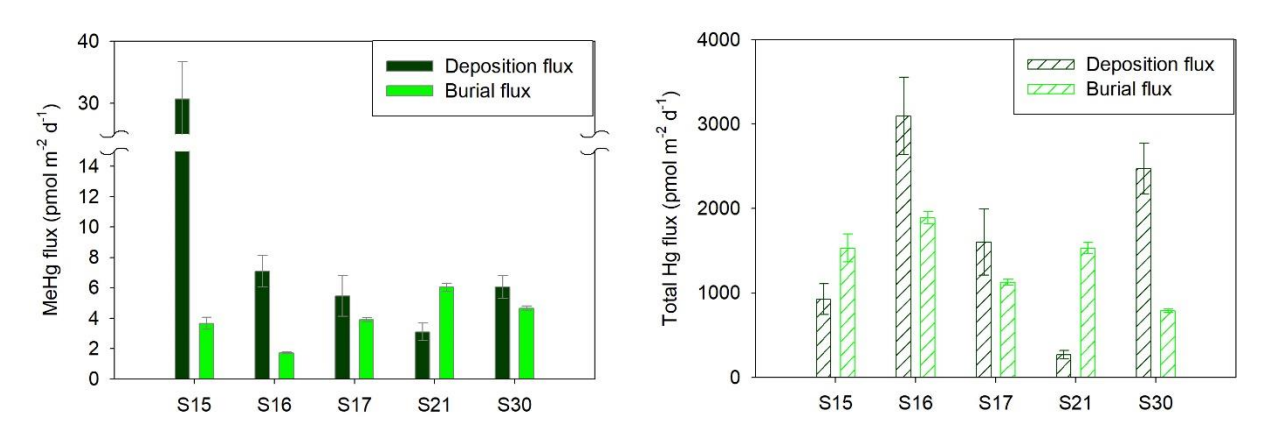


Fig. 4 Deposition flux (estimated from <sup>234</sup>Th<sub>ex</sub>) and burial flux (estimated from <sup>228</sup>Th<sub>ex</sub>) of MeHg (left) and total Hg (right) at the sediment-water interface.

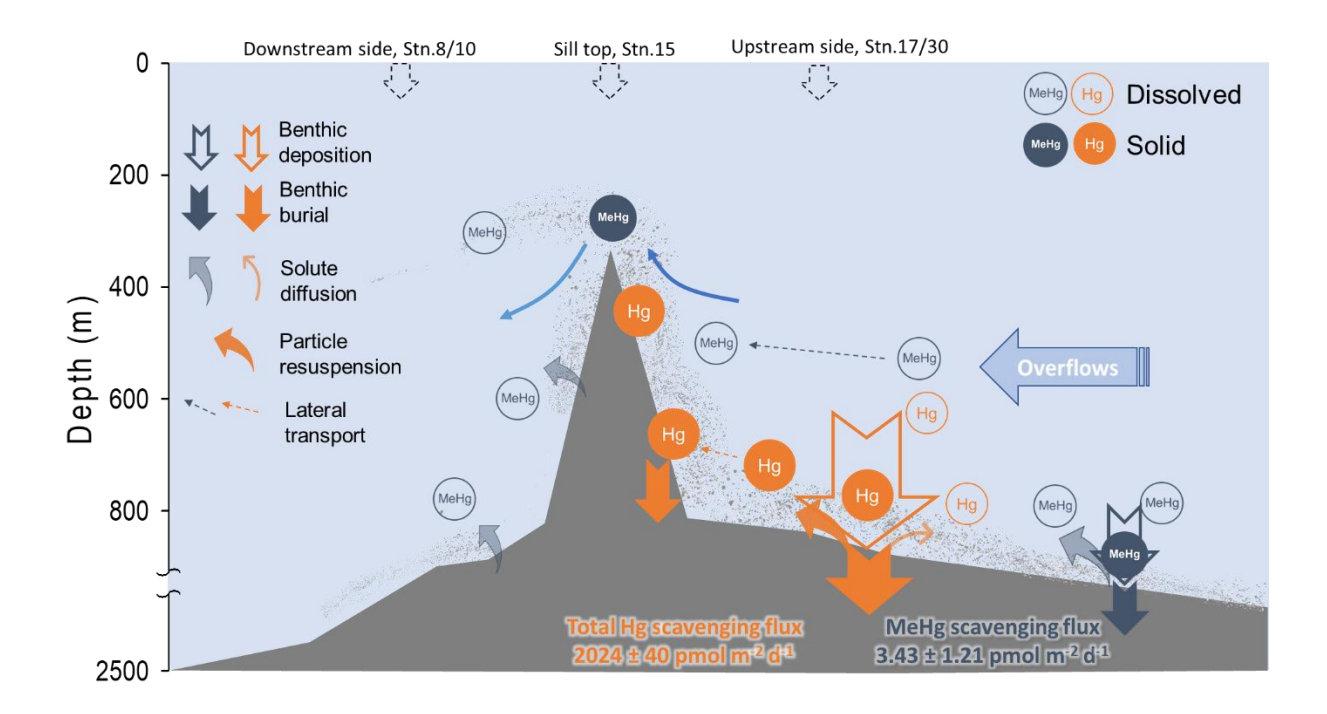


Fig. 5 The schematic of benthic processes to Hg species during the entrainment with the overflows in the regions around Iceland. The solid circles represent solid phase and the open circles refer to dissolved phase. The orange and indigo colors stand for total Hg and MeHg, respectively. The legends on the left indicate the specific processes across the sediment-water interface. The net benthic scavenging fluxes are shown in the bottom.